ORIGINAL ARTICLE

lajss.org
Latin American Journal of Solids and Structures

www.lajss.org

Research on static tensile properties and damage mechanism of GLARE laminates

Tong Anshi[a], Zhang Jun[a*], Wang Danfeng[a], Chen Ying[a], Xie Liyang[b]

[a]School of Mechanical Engineering, Shenyang University, Shenyang, China. Email: tonganshi680@163.com, zhjun88@126.com, wang2011823@126.com, chenyinghappyday@163.com
[b]School of Mechanical Engineering and Automation, Northeastern University, Shenyang, China. Email: lyxie@mail.neu.edu.cn

* Corresponding author

https://doi.org/10.1590/1679-78258122

Abstract

To study the variation law of static tensile properties and damage mechanism of fiber metal laminates, this paper conducted static tensile tests on six types of GLARE specimens. During the testing process, the full-field strain data of the specimen were captured using Digital Image Correlation technology. A comparative analysis was conducted on the elastic modulus, tensile strength, stress-strain curve, and Poisson's ratio change curve. The fracture morphology of the specimen, strain cloud map before final fracture, and the process of strain difference formation were compared and analyzed. The results show that the bridging effect of fibers needs to be properly considered when using the hybrid model method to predict the tensile strength of the ±45°fiber-metal laminates. The role of the prepreg layer in the GLARE sample gradually increases after the metal material yields. For the same type of prepreg, the damage forms in different layers of the board are not exactly the same. Using the DIC method is helpful to study the damage process and boundary effects inside the fiber metal laminate.

Keywords

Fiber metal laminate, GLARE, Tensile properties, Damage mechanism, Digital image correlation technology

Graphical Abstract

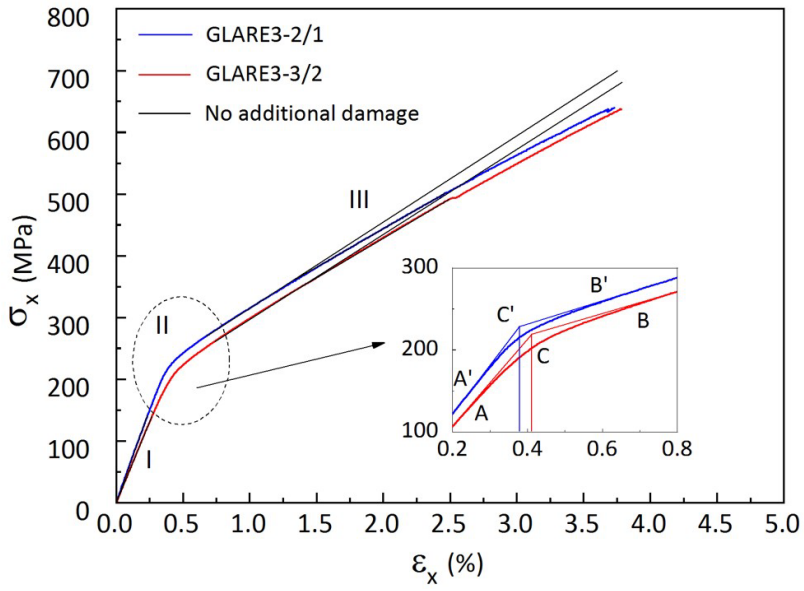

Received March 24, 2024. In revised form August 09, 2024. Accepted September 06, 2024. Available online September 10, 2024.
https://doi.org/10.1590/1679-78258122

1 INTRODUCTION

Since the 1950s, aerospace technology has developed rapidly, and in the industry, the requirements for the performance of structural materials have become increasingly higher. Traditional aluminum alloy materials are easy to process and have good impact resistance, but have poor fatigue performance and corrosion resistance. Fiber-reinforced composite materials have higher strength and fatigue resistance, but have poor ductility and impact resistance, and is difficult to process. In the 1970s, Delft University of Netherlands combined the advantages of the above two materials and first proposed the concept of fiber metal laminates. Fiber Metal Laminates (FMLs) are a type of hybrid material formed by the alternating stacking of metal layers and fiber-reinforced composite layers, which are cured at a certain temperature and pressure[1]. It has the advantages of excellent fatigue damage tolerance, impact resistance, corrosion resistance, high flame retardancy and easy processing and molding[2-4]. It mainly includes four types, including ARALL (Aramid Reinforced Aluminum Lamiantes), GLARE (Glass Reinforced Aluminum Lamiantes), CARE (Carbon Reinforced Aluminum Lamiantes) and TIGR (Titanium/GraphiteHybridLamiantes)[5-7].

Its mechanical properties, different from those of metal materials, are anisotropic and are affected by various factors such as component material properties, lamination type, molding process, specimen size, and load environment.

Its damage mechanisms and mechanical property curve are different from those of metal materials. In terms of fatigue performance, although the total life of FMLs is much longer than that of metallic materials, the crack initiation life is likely to be shorter than that of metallic materials[8,9]. In terms of static properties, the tensile strength of FMLs is much greater than that of metal materials, but the yield strength is likely to be less than that of metal materials. At the same time, the dispersion of data and the sensitivity to gaps are also greater than that of metal materials[10,11]. In addition, the damage process of fiber metal laminates is more complicated, often starting from the inside, and it is not easy to detect the damage process by simple visual inspection[12,13]. As a designable structural material used in aircraft skin, it urgently needs to reduce weight and ensure safety during the life cycle. Therefore, it is necessary to study in detail the changing rules and evaluation methods of mechanical properties of fiber metal laminates, and damage detection methods of fiber metal laminates.To this end, many scholars are involved. In terms of the static properties of fiber metal laminates, Wu and Yang[14] conducted static tensile tests in one direction on GLARE4-3/2 and GLARE5-2/1. Carrillo and Cantwell[15] studied the size effect of fiber metal laminates by changing the sample size. Rajkumar et al.[16] conducted static tensile tests at speeds of 1, 2 and 3 mm/min on various fiber metal laminates mixed with glass fiber and carbon fiber. Wang[17] conducted static tensile tests on two types of glass fiber aluminum alloy plates with unidirectional and orthogonal fiber laying; Yang[18] studied the effects of fiber arrangement angle, component volume fraction, component type and mixed layer fiber on the static tensile properties of fiber metal laminates. Dadej et al.[19] studied the effect of the mixed volume ratio of carbon fiber and glass fiber on the static tensile strain of metal fiber laminates. He et al.[20] studied the experimental characterization and numerical prediction of the tensile mechanical behavior and failure mechanism of porous fiber metal laminates. Yao et al.[21] studied the tensile mechanical behavior and failure mechanism of fiber-metal laminates under different temperature environments. Yong et al.[22] studied the effect of hygrothermal aging on moisture diffusion and tensile properties of CFRP composite laminates. Sun et al.[23] studied the mechanical response of fiber metal laminates under low to medium strain rate tension. Kötter et al.[24] used digital image correlation (DIC) system to in-situ evaluate the strain field on the surface of CFRP thin fiber metal laminates when studying the effects of layer thickness and metal layer on the tensile and compressive properties of the openings. Xu et al.[25] combined acoustic emission and DIC technique to study the in-situ damage assessment of FML joints under uniaxial tension. Zheng et al.[26] characterized the damage mode and evolution of porous GLARE laminates under tensile load by integrating AE and DIC technologies. Jakubczak, Serubibi and Abhishek et al.[27-29] used the DIC method to study the impact damage of fiber metal laminates. Romanowicz et al.[30] concluded that DIC technique can be successfully applied for the analyses of hybrid steel/adhesive/ composite samples.

This paper focuses on studying the changing rules of the stress-strain curve and Poisson's ratio of GLARE laminates under static tensile load, analyzing the applicability of using the hybrid model method to predict the elastic modulus and tensile strength of GLARE laminates, and exploring the use of digital image correlation technology in real-time observation of the damage process of the prepreg layer. For this purpose, six types of GLARE specimens were selected for static tensile testing, namely GLARE2-2/1, GLARE2-3/2, GLARE3-2/1, GLARE3-3/2, GLARE6-2/1 and GLARE6-3/2. During the test, the load data of the specimen was recorded, and the full-field strain data of the specimen at different loading stages was recorded using DIC. The axial and lateral strain data at the specimen section were recorded using a strain gauge. After the test, the fractured specimen was subjected to corrosion delamination analysis. The results of this study will be beneficial to improving the use efficiency and material performance of FMLs, and improving the efficiency and accuracy of fault diagnosis. The specific data acquisition methods and analysis process are as follows.

2 Trial test

2.1 Materials and samples

The GLARE specimens used for testing , as shown in Figure 1, are constructed by alternating layers of 2024-T3 aluminum alloy and S4/SY-14 prepreg layers. The layup form of the samples is shown in Table 1, mainly including GLARE2-2/1, GLARE2-3/2, GLARE3-2/1, GLARE3-3/2, GLARE6-2/1 and GLARE6-3/2. The mechanical properties of the component materials are shown in Table 2. The geometric form and size of the samples are shown in Figure 2. The total length L=270mm, the gauge section length L_G=160mm, and the width W=15mm meet the ASTM D-3039 standard. In order to prevent the samples from being damaged at the clamping point during the loading process, aluminum alloy reinforcement sheets with a thickness of 0.25 mm are affixed to both ends.

Figure 1 Test specimen.

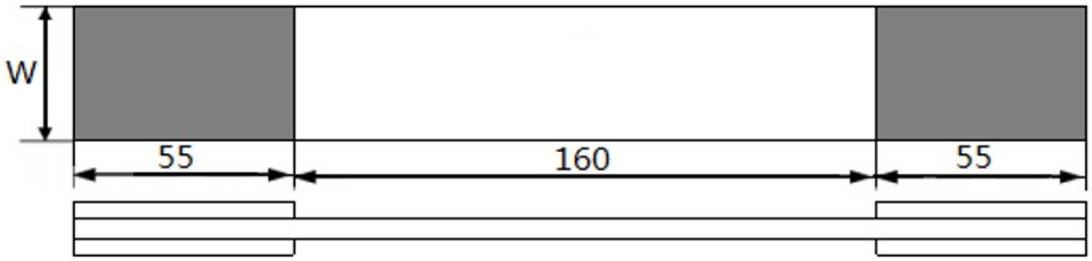

Figure 2 Geometry and dimensions of specimens.

Table 1 Type of GLARE laminates.

Laminates	Ply scheme	Thickness of aluminum/mm	Average thickness of prepreg/mm
GLARE2-2/1	Al/0/Al	0.262	0.271
GLARE2-3/2	Al/0/Al/0/Al	0.252	0.295
GLARE3-2/1	Al/90/0/Al	0.262	0.273
GLARE3-3/2	Al/90/0/Al /0/90/Al	0.245	0.282
GLARE6-2/1	Al/+45/-45/Al	0.247	0.296
GLARE6-3/2	Al/+45/-45/Al/-45/+45/Al	0.254	0.288

Table 2 Mechanical properties of component materials.

Material type	Tensile strength/MPa	Shear strength/MPa	Poisson's ratio v_{12}	Elastic modulus/GPa	Shear modulus/GPa
0° Prepreg	1900	129	0.3	50	5.3
90° Prepreg	62.2	129	0.063	10.5	5.3
2024-T3 Aluminum alloy	463.3	-	0.33	72	27.2

2.2 Digital image correlation technologies

DIC is a non-contact and non-destructive image evaluation technology, which can effectively track the surface displacement of deformed materials[31]. Its working principle is[32]: At the beginning of the test, the CCD camera collects the image before deformation as a reference object, and then collects the image of deformation under a certain load. The deformation of the sample under this load can be obtained by monitoring and comparing the displacement changes of the given grid points in the two images. Then the damage inside the sample can be determined based on the difference in deformation. Comparing with other measurement methods such as ultrasonic C-scan and corrosion delayering method, DIC is considered to be the most rapid and effective non-destructive testing method. This testing method is not limited to the sample form, the number of collected images, the size and shape of the grid, and the damage status can be collected at any time during the test to obtain the form and change process of internal damage. It is also simple to operate and easy to use. Therefore, it has good application prospects in measuring the damage mechanism of fiber metal laminates.

2.3 Experimental testing process

The test site is shown in Figure 3. It was conducted on a Shimadzu static tensile testing machine (SHIMADZU300kN), using strain control, under a loading speed of 2mm/min. A strain gauge was attached in the middle of the sample to record the axial and transverse strains simultaneously during the stretching process. The DIC equipment used for testing is ARAMIS 4M produced by GOM Formula. During the stretching process, sampling is performed by taking photos evenly, and each sample were taken at least 30 photos. After the test, 4% sodium hydroxide solution was used to remove the aluminum alloy layer in the sample.

Figure 3 Test of GLARE laminates under tensile loading.

3 Results and discussions

3.1 Elastic modulus and tensile strength

3.1.1 Elastic modulus

The ROM[33] formula is used to calculate the axial elastic modulus E_{h1} of the GLARE sample, which is:

$$E_{h1} = (MTF \times E_{Al}) + (1 - MTF) \times E_{frp} \quad (1)$$

Where the E_{h1} is the elastic modulus of the laminate. MTF is the volume fraction of the aluminum alloy layer. E_{Al} is the elastic modulus of the aluminum alloy layer;E_{frp} is the elastic modulus of the prepreg layer. The data required for calculation are shown in Table 1 and Table 2, and the calculation results are shown in Table 3 and Figure 4. The results show that the calculated value of the axial elastic modulus of the GLARE2 and GLARE3 samples is close to the tested value, with an error less than 1%; the calculated value of the GLARE6 laminate is lower than the tested value, with an error of about 5%.

3.1.2 Tensile strength

The ROM[33] formulais used to calculate the tensile strength σu of the GLARE sample, which is:

$$\sigma_u = (MTF \times \sigma_{\mathrm{Al}}) + (1 - MTF) \times \sigma_{frp} \quad (2)$$

Where the σ_u is the tensile strength of the laminate. MTF is the volume fraction of the aluminum alloy layer. σ_{Al} is the tensile strength of the aluminum alloy layer. σ_{frp} is the tensile strength of the prepreg layer. The data required for calculation are shown in Table 1 and Table 2, and the calculation results are shown in Table 4 and Figure 5. The results show that when the prepreg is laid in the 0° direction, the tensile strength of GLARE specimens increases with the number of layers. However, when the prepreg is laid in the 0°/90° and ±45° directions, the tensile strength of GLARE specimens decreases with the increase in the number of layers. The tensile strengths of GLARE6, 3, and 2 samples are approximately 1, 1.5, and 2.5 times that of the aluminum alloy respectively. The calculation error of the tensile strength for GLARE2 and 3 specimens is within 5%, and it is easy to underestimate when laying 1/2 and to overestimate when laying 2/3. Calculating the tensile strength of GLARE6 laminates based on the shear strength of the prepreg will significantly underestimate the test results. Taking into account the bridging effect, using 2 times the shear strength is close to the test results.

Table 3 Elastic modulus of GLARE laminates.

Specimen	Theoretical value/GPa	Experimental value/GPa	Relative error/%
G2-2/1	63.91	64.14	-0.36
G2-3/2	62.36	62.48	-0.19
G3-2/1	59.18	59.32	-0.24
G3-3/2	53.87	53.35	0.97
G6-2/1	46.92	48.58	-3.44
G6-3/2	43.43	45.62	-5.19

Table 4 Tensile strength of GLARE laminates.

Specimen	Theoretical value/GPa	Experimental value/GPa	Relative error/%
G2-2/1	952.84	979.30	-2.78
G2-3/2	1092.89	1038.94	4.94
G3-2/1	640.43	667.38	-4.21
G3-3/2	687.91	663.08	3.61
G6-2/1	386.19	389.33	-0.81
G6-3/2	374.78	373.49	0.34

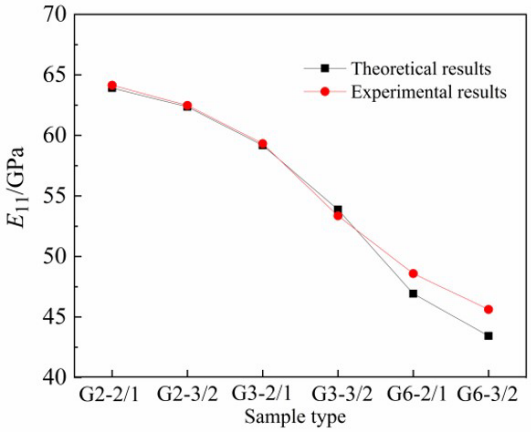

Figure 4 Elastic modulus of GLARE laminates.

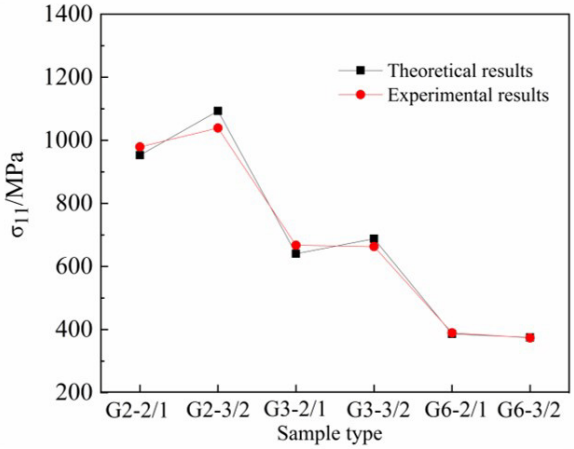

Figure 5 Tensile strength of GLARE laminates.

3.2 Stress-strain curve

In general, the stress-strain curve of the GLARE laminate can be divided into four stages: I is the linear elastic stage. The aluminum alloy layer and the prepreg layer share the load. II is the transition stage. The aluminum alloy layer yields and the laminate loses part of the load-bearing capacity. III is the re-stabilization stage. The effect of the prepreg layer becomes more obvious as the load increases. IV is the fracture stage. The laminate eventually loses its load-bearing capacity due to the fracture of the prepreg layer.

In Figure 6a, the deflection process of the stress-strain curve of the GLARE2 sample is close to bilinear. The strains of GLARE2-2/1 and GLARE2-3/2 samples in the transition stages A'B' and AB are 0.246%-0.501% and 0.258%-0.518% respectively, and the corresponding stresses are 159-261MPa and 157-257MPa respectively. In the re-stabilization stage, the slope of the stress-strain curve of the GLARE2-3/2 sample is higher than that of the GLARE2-2/1 sample. The reason is that the proportion of the 0°direction prepreg layer which plays the main load-bearing role is higher, but it is lower than the case without any other damage, indicating that the load-bearing capacity of aluminum alloy has decreased.

In Figure 6b, the turning process of the stress-strain curve of the GLARE3 laminate is also close to bilinear. The strains of GLARE3-2/1 and GLARE3-3/2 samples in the transition stages A'B' and AB are 0.236%-0.677% and 0.267%-0.734% respectively, and the corresponding stresses are 143-270MPa and 141-262MPa respectively. In the re-stabilization stage, the slope of the stress-strain curve of GALRE3-3/2 and GALRE3-2/1 samples is the same, which is quite different from the case without other damage, and presents three linear change stages, indicating that the 90°direction prepreg layer was damaged during the loading process.

In Figure 6c, the deflection process of the stress-strain curve of the GLARE6 sample is gentler. The strain ranges of GLARE6-2/1 and GLARE6-3/2 samples in the transition stages A'B' and AB are 0.276%-0.960% and 0.299%-1.099% respectively, and the corresponding stresses are 137-221MPa and 135- 218MPa respectively. In the re-stabilization stage, the slopes of the stress-strain curves of the GALRE6-2/1 and GALRE6-3/2 samples are the same, showing a multi-segment linear change, which is quite different from the case without additional damage, indicates that the effect of the ±45° prepreg layers on the enhancement of axial load-bearing capacity is limited.

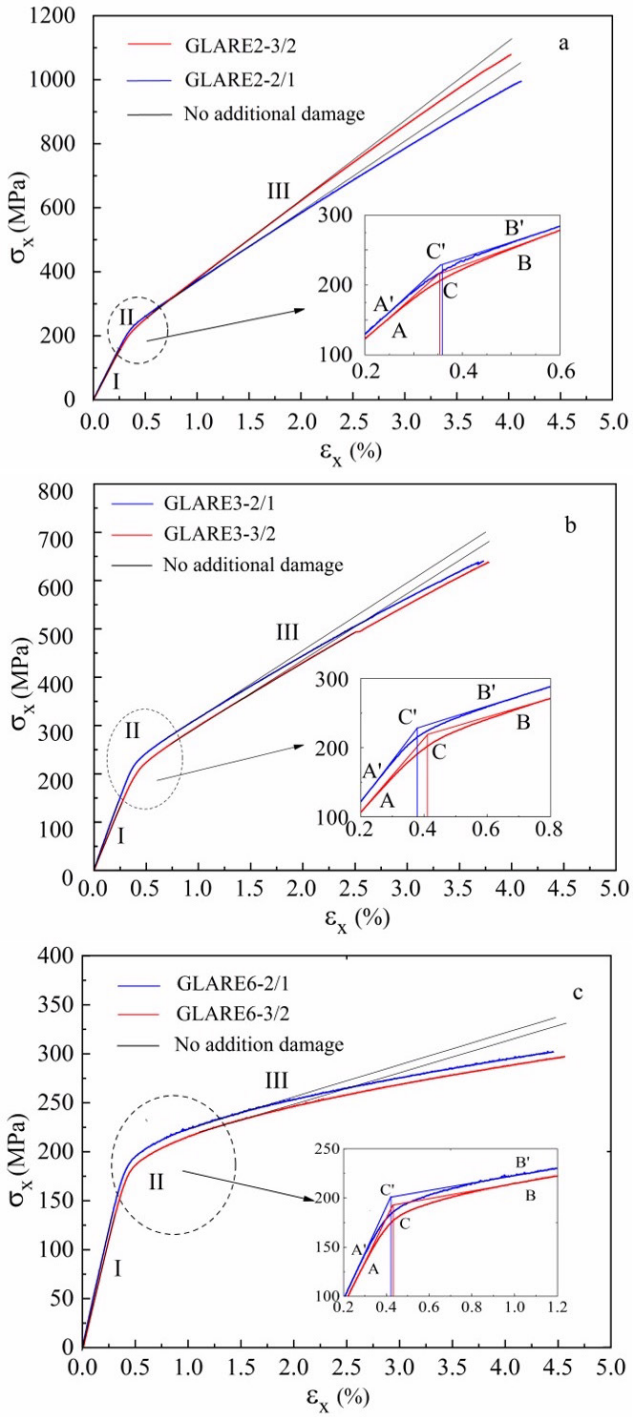

Figure 6 Stress–strain curves of GLARE laminates under uniaxial tensile loading. (a) GLARE2-2/1 and 3/2;(b) GLARE3-2/1 and 3/2;(c) GLARE6-2/1 and 3/2

3.3 Poisson's ratio-axial strain curve

In general, the axial Poisson's ratio-axial strain curve of the GLARE sample can be divided into three stages: I stable stage, the aluminum alloy layer is in the linear elastic stage. II transition stage, the aluminum alloy layer is in the yield stage. III rapid change stage, the role of the prepreg layer is more prominent than I and II stage.

The GLARE2-3/2 sample is in coincident with GLARE2-2/1 sample. In Figure 7a, the Poisson's ratio v_{xy} of the GLARE2-2/1 sample changes steadily within the axial strain range of 0.27%, with an average value of approximately 0.322. In the strain range of 0.27%-0.93%, the yield of the metal layer rapidly increases to around 0.361%, and then gradually dropped to around 0.34 due to the increased effect of the prepreg layer in the 0°direction. The conditions of GLARE2-3/2 and GLARE2-2/1 samples are basically the same.

In Figure 7b, the Poisson's ratio v_{xy} of the GLARE3-2/1 sample changes steadily within the axial strain range of 0.27%, with an average value of approximately 0.305. It rises slightly to around 0.308% within the axial strain range of 0.27%-0.33% , and then quickly dropped to around 0.25. The Poisson's ratio of the GLARE3-3/2 sample has no obvious rising process and gradually decreases to around 0.14 after the axial strain of 0.27. The reason is that the role of the 90° prepreg layer increases during the yielding process of the metal layer, which offsets the increase in Poisson's ratio during the plastic deformation stage of the aluminum alloy layer.

In Figure 7c, the Poisson's ratio v_{xy} of the GLARE6-3/1 sample increases slightly in the axial strain range of 0.335%, with an average value of 0.365. After the metal layer yields, it gradually rises to around 0.51. The situations of GLARE6-3/2 and GLARE6-2/1 samples are basically the same. Affected by the increase in the proportion of ±45°prepreg layer, the Poisson's ratio at each stage is higher and its rising speed is faster.

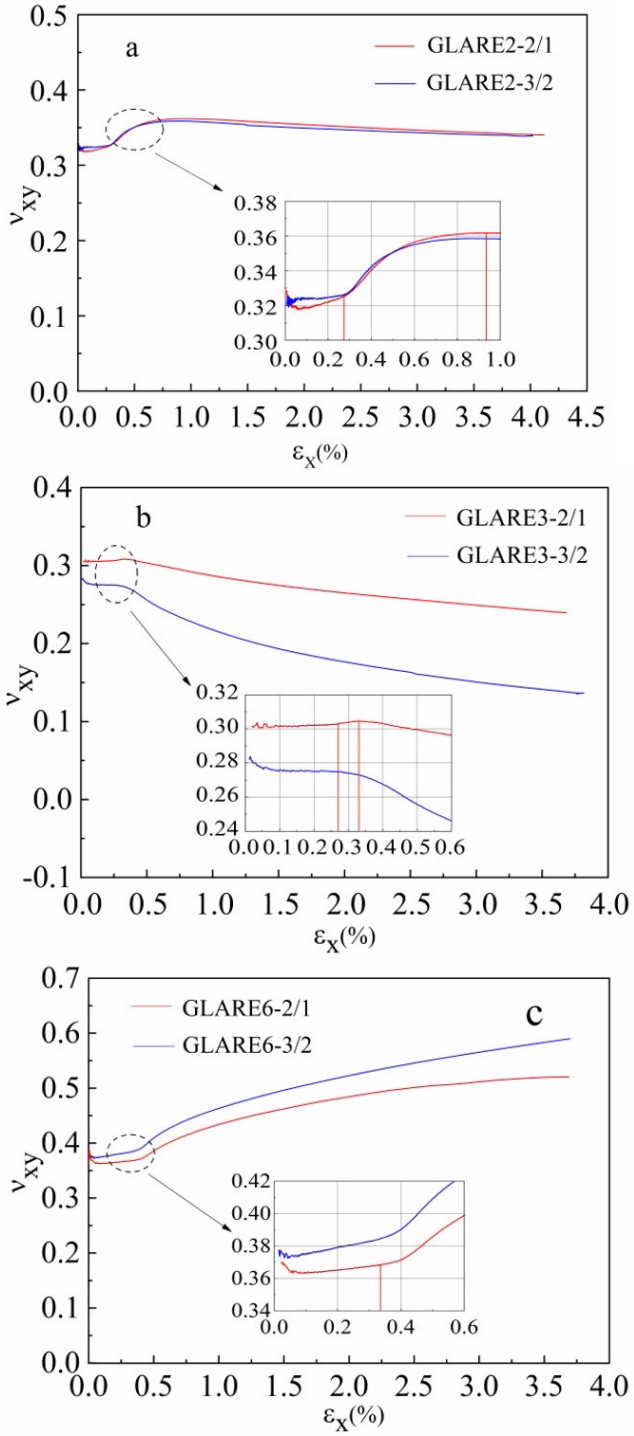

Figure 7 Poisson's response of GLARE laminates. (a) GLARE2-2/1 and 3/2;(b) GLARE3-2/1 and 3/2;(c) GLARE6-2/1 and 3/2

4 Samples damage patterns

4.1 Fracture process and damage morphology

Fig 8(a-f) shows the damage morphology of the GLARE2-2/1, GLARE2-3/2, GLARE3-2/1, GLARE3-3/2, GLARE6-2/1 and GLARE6-3/2 specimen.

In Fig 8a, the 0° prepreg layers of the two GLARE-2/1 specimen were all broken, but the metal layers remained intact. During the test, the sound of a small amount of fiber breaking was heard first, and then the laminates were instantly delaminated. In Fig 8b, the fracture forms of the GLARE2-3/2 specimens include two kinds, fracture near the clamping point and direct delamination. The damage of the 0° prepreg layer is more regular than that of the GLARE2-2/1 specimen. No sound of fiber fracture was heard during the test, and the laminate was directly broken. In general, the fracture of the 0° prepreg layer is the direct cause of the final failure of the GLARE2 specimen. When the number of layer is large, the laminate is more likely to break instantly, and when the number of layer is small, it is more likely to delaminate.

In Fig 8c, the fracture forms of the GLARE3-2/1 specimen include two kinds, fracture near the clamping point and direct delamination. Due to the asymmetry of the prepreg layer, the fractured specimen has obvious bending. During the loading process, a small amount of fiber fracture sound was heard first, and then the laminate broke instantly. In Fig 8d, the fracture of all the GLARE3-3/2 specimens occurred near the clamping point. Compared with the GLARE3-2/1 specimens, the damage form of the internal prepreg layer was more uniform. No fiber fracture sound was heard during the loading process, and the specimen broke directly. In general, the fracture of the prepreg layer in the 0° direction will directly lead to the final failure of the GLARE3 specimen. When the number of layer is large, the laminate is more likely to break instantly, and when the number of layer is small, it is more likely to delaminate.

In Fig 8e, the fracture of the GLARE6-2/1 specimen occurred in the middle of the specimen, with severe bending. When it finally broke, the fiber and the metal broke at the same time, without any sound signal. In Fig 8f, the fracture of the GLARE6-3/2 specimen include two locations: near the clamping point and in the middle. The fracture form of the specimen is regular without bending. There is no sound signal during the fracture process of the specimen, and the fiber and metal are broken simultaneously. In general, the shear fracture of the fibers and matrix of the ±45° prepreg layer will directly lead to the final fracture of the GLARE6 specimen. The brittleness of the specimen increases with the number of layers, and it is easier to bend when the number of layers is small.

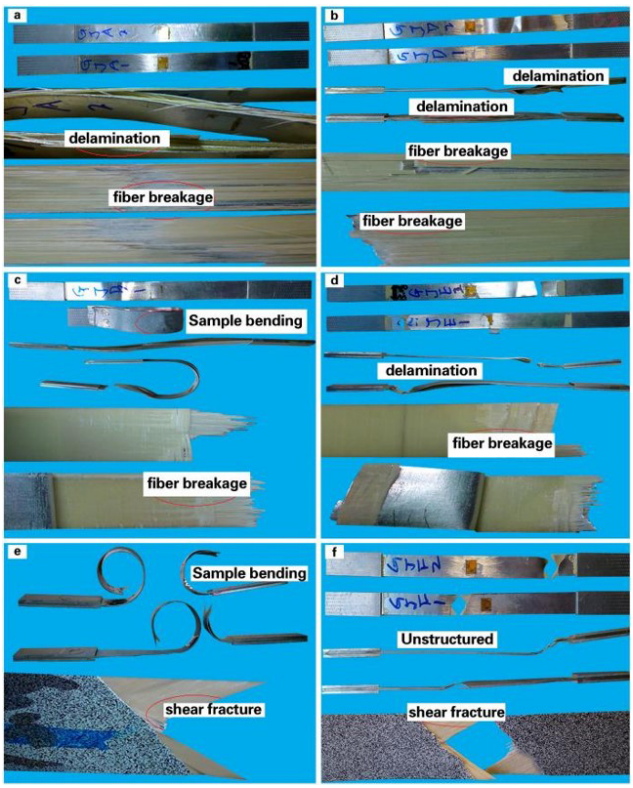

Figure 8 The fracture mode of GLARE laminates samples. (a) GLARE2-2/1;(b) GLARE2-3/2;(c) GLARE3-2/1;(d) GLARE3-3/2;(e) GLARE6-2/1;(f) GLARE6-3/2

4.2 Damage patterns of prepreg layers

The aluminum alloy layer in the sample was removed by etching to obtain the damage pattern of the internal prepreg layer, as shown in Figure 9(a-f).

In Figure 9a, the 0°direction prepreg layer in the GLARE2-2/1 sample is completely broken. Figure 9b, the 0°direction prepreg layer in the GLARE2-3/2 sample breaks neatly.

In Figure 9c, tthe damage form of 0°direction prepreg layer of the GLARE3-2/1 specimen is fiber breakage and pull-out, the 90°direction prepreg layer in the GLARE3-2/1 sample contains a large number of uniform matrix microcracks. In Figure 9d,the damage form of the 0° prepreg layer of the GLARE3-3/2 specimen is the same as that of the GLARE3-2/1 specimen,the number and extent of matrix microcracks in the 90°direction prepreg layer in the GLARE3-3/2 sample are much smaller than those in the GLARE3-2/1 sample.

In Figure 9e, the±45°direction prepreg layer in the GLARE6-2/1 sample contains matrix microcracks, and the damage form at the fracture is mainly matrix shear fracture. In Figure 9f, the cracking degree of the matrix cracks in the prepreg layer in the GLARE6-3/2 sample is much greater than that in the GLARE6-2/1 sample, and the damage pattern at the fracture also includes a certain amount of fiber tensile fracture.

Generally speaking, for laminates with prepreg layers in the same direction, different numbers of layers cause slightly different damage mechanisms or degrees, which is mainly reflected in the different load sizes and fiber bridging effects at fracture.

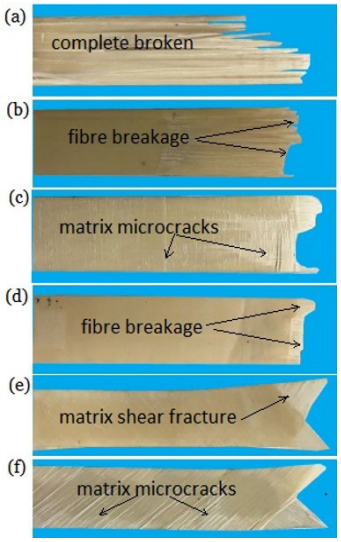

Figure 9 Damage characteristics of glass/epoxy prepreg after removal of outer aluminium layers. (a) GLARE2-2/1;(b) GLARE2-3/2;(c) GLARE3-2/1;(d) GLARE3-3/2;(e) GLARE6-2/1;(f) GLARE6-3/2

5 DIC test results and analysis

5.1 The formation process of strain cloud diagram and strain difference

The axial and transverse strain cloud diagrams of GLARE2,3,6-3/2samples before final fracture,and the formation process of strain differences at key locations, are shown in Figure 10. The strain zone length L_G=40mm, and the width W=15mm.

In Fig 10 a and b, the axial strain and transverse strain in the gauge section of the GLARE2-3/2 specimen are basically uniform, and the strain difference is small, indicating that there is no obvious matrix crack and interlayer delamination damage in the specimen at this time. In Fig 10c, the axial strains at the three positions *A*, *B*, and *C* of the GLARE2-3/2 specimen remain consistent and show a stable linear relationship with the load. However, after an axial strain of about 1.7%, the lateral strain at the boundary point B begins to gradually exceed that at the middle position of the specimen, and gradually increases with the increase in load, indicating that the damage of the specimen first occurs at the boundary and gradually expands.

In Fig 10d, the axial strain cloud diagram of the GLARE3-3/2 specimen in the gauge section shows uniform transverse stripes, and the strain difference is obvious, indicating that at this time, there is uniform transverse stripe damage in the 90° prepreg layer of the laminate, but there is no large-scale interlayer delamination damage. In Fig 10e, the lateral strain at the boundary of the GLARE3-3/2 specimen is significantly larger, which means that the boundary of the specimen is affected by a greater lateral shear force during loading. In Fig 10f, the load-bearing capacity of the GLARE3-3/2 specimen has a short-term enhancement near the axial strain of 0.3%, corresponding to the yielding of the metal layer and the 0° direction

prepreg layer starting to bear the main load. After that, a strain difference begins to appear at the positions of points *D* and E of the stripes around the axial strain of about 1.3%, and increases with the load. The material properties undergo a rapid degradation process around the axial strain of about 2%, and then the strain difference at points *D* and E remains basically unchanged. In Fig 10f, the transverse strain at *D*, *E* and *F* three positions of the GLARE3-3/2 specimen is close to a linear relationship with the load. The transverse strain at the boundary point F is higher than that in the middle of the specimen from the initial stage, and the strain difference increases with the load. The above phenomenon shows that the damage process of the matrix in the 90° prepreg layer of the GLARE3-3/2 specimen is gradual, and tends to be stable after instantaneous degradation, and the boundary of the specimen is subjected to a greater transverse shear force.

In Fig 10g and h, the axial and transverse strains in the gauge section of the GLARE6-3/2 specimen are very uneven, with a large strain gradient, and the overall shape is ±45° stripes, indicating that ±45° matrix microcrack damage and local delamination damage have occurred in the prepreg layer. In Fig 10h, the transverse strain at the boundary of GLARE6-3/2 specimen is smaller, which is opposite to the situation of GLARE2-3/2 and GLARE3-3/2 specimens. In Fig 10i, the axial strains at *G*, *H* and *I* three positions of the GLARE6-3/2 specimen are always consistent. After about 2.5% axial strain, the transverse strain at the boundary point I begins to be lower than that at the middle position of the specimen. At about 5% and 7.5% axial strain, the axial and transverse properties of the specimen simultaneously show twice instantaneous degradation phenomena. The above phenomena indicate that the damage process of the prepreg layer in the GLARE6-3/2 specimen is a process from gradual to instantaneous, then gradual and then instantaneous.

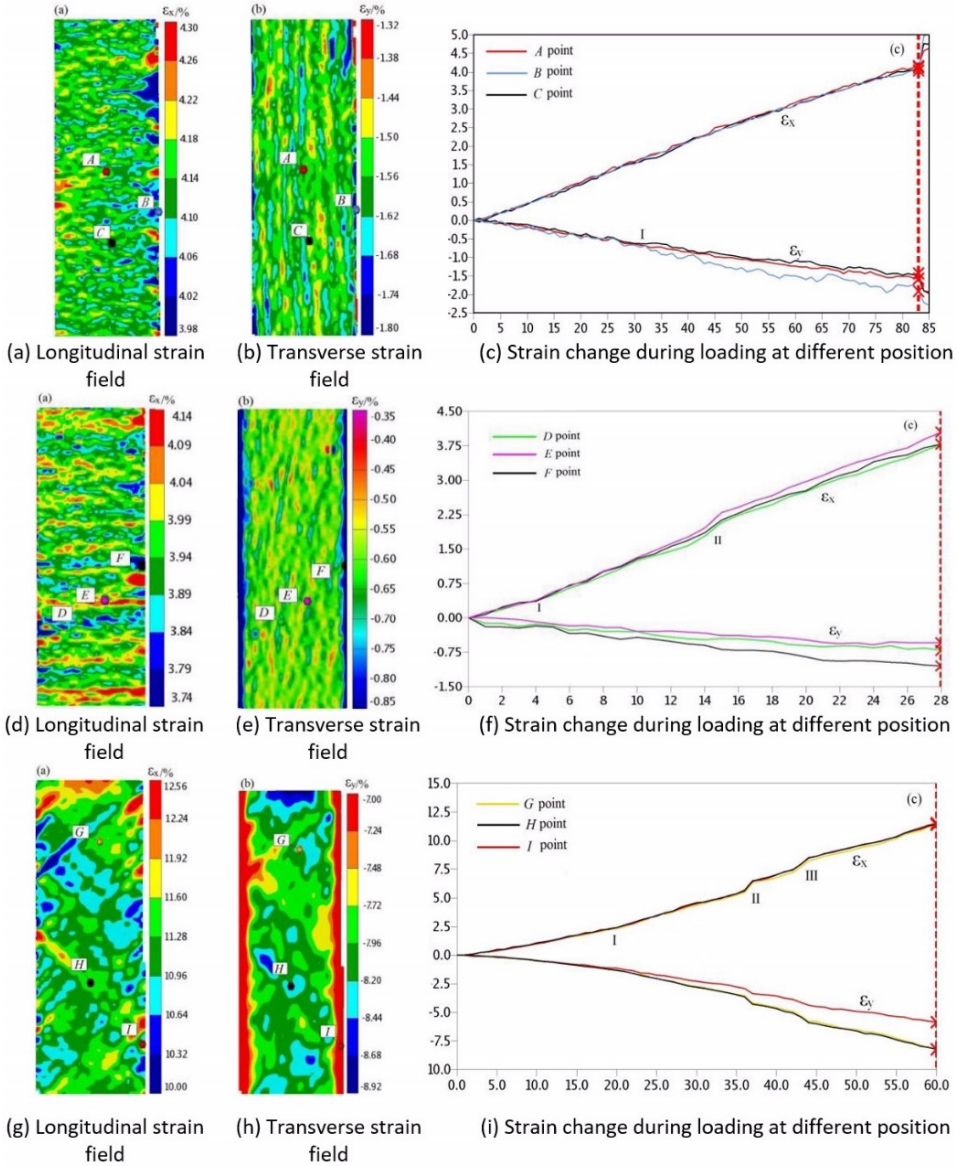

Figure 10 Surface longitudinal strain field (ε_x) and transverse strain (ε_y) of representative GLARE2,3,6-3/2 specimens obtained with the DIC technique at the stage before failure and the strain variation during loading at different position.

5.2 Strain change process at mid-section

The change processes of axial and transverse strain at the mid-sectional position of the GLARE2-3/2, GLARE3-3/2 and GLARE6-3/2 samples are shown in Figure 11(a-f).

In Figure 11a, the axial strain at the mid-sectional position of the GLARE2-3/2 sample remains basically the same. In Figure 11b, the transverse strain at the mid-section of the GLARE2-3/2 sample appears wavy even from the initial stage of loading, which shows that the elastic modulus of the resin and fiber in the prepreg layer is different. The transverse strain at the boundary increased rapidly in the later stage of loading, indicating that small delamination damage occurred.

In Figure 11c, the axial deformation at the mid-sectional position of the GLARE3-3/2 sample also remains consistent. In Figure 11d, the transverse strain at the mid-section of the GLARE3-3/2 sample also appears wavy in the initial stage of loading, and the location within 3 mm of the boundary is subject to greater transverse stress.

In Figure 11e, the axial strain within 2 mm of the boundary of the GLARE6-3/2 specimen increased rapidly before the final fracture, indicating that delamination and other damage occurred. In Fig11f, the lateral strain amplitude within 1.5 mm of the boundary of the GLARE6-3/2 specimen is smaller than that in the middle of the specimen. The overall shape is U-shaped and becomes more obvious with the increase of load, indicating that the GLARE6-3/2 specimen has poor ability to resist lateral deformation and the boundary is less affected by lateral force.

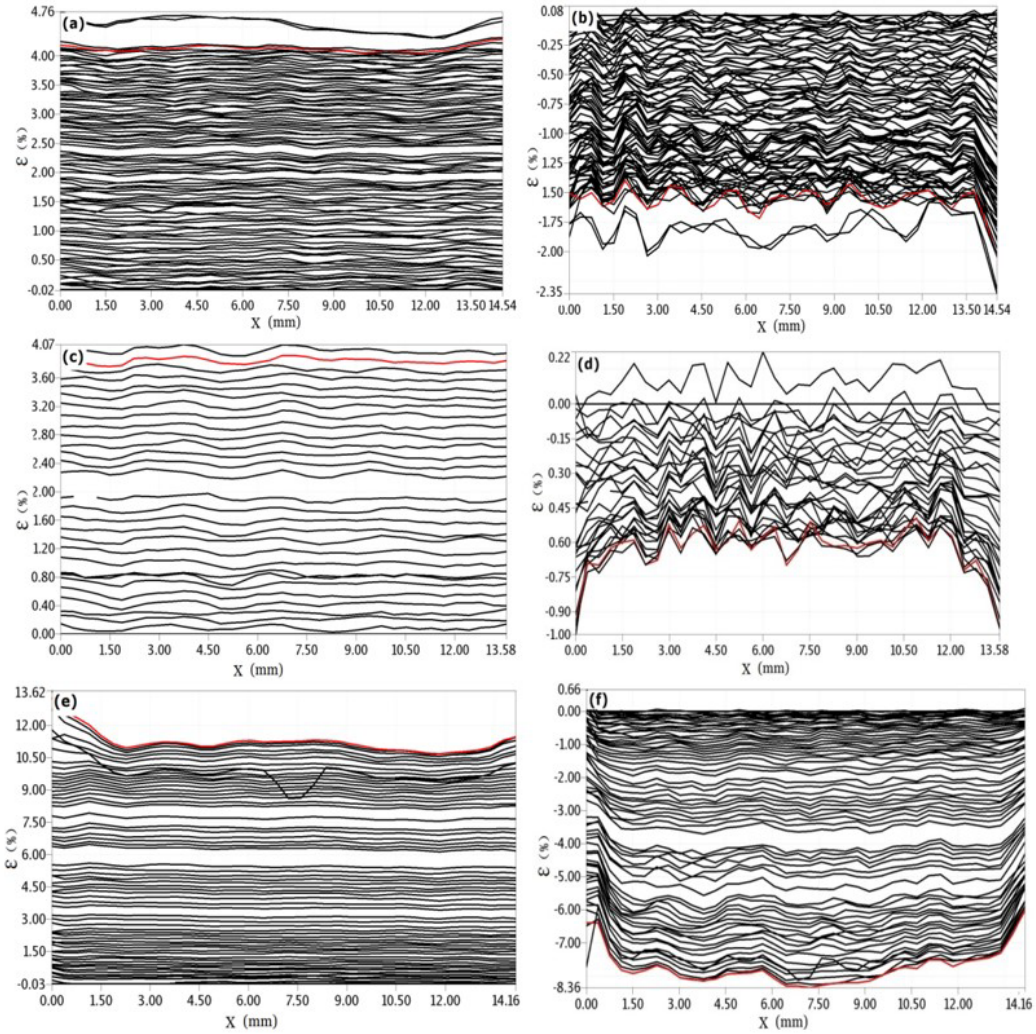

Figure 11 Strain curves of GLARE laminate at middle position under uniaxial tensile loading. (a) GLARE2-3/2-ε_x ; (b) GLARE2-3/2-ε_y; (c) GLARE3-3/2-ε_x ;(d) GLARE3-3/2-ε_y;(e) GLARE6-3/2-ε_x;(f) GLARE6-3/2-ε_y

6 CONCLUSION

(1) The hybrid model method was used to calculate the elastic modulus and tensile strength of the GLARE2 and GLARE3 samples, which is close to the test results. The calculated elastic modulus of the GLARE6 sample is lower than the

test value with an error of about 5%. When calculating the tensile strength, considering the bridging effect by taking 2 times the shear strength can obtain calculated results close to the test results.

(2) The stress-strain curve of the GLARE laminate gradually enters the transition stage after the axial strain of 0.236%, and gradually enters the stable stage again after the axial strain of 0.5%. Regardless of the layup form, the load-bearing capacity of GLARE samples decreases during the re-stabilization stage. When laid at ±45°, the load-bearing capacity decreases most obviously and its value is close to that of the pure metal state.

(3) The Poisson's ratio v_{xy} of the GLARE sample is basically stable at the axial strain lower than 0.27%. During the yielding process of the metal layer, the Poisson's ratio increases, but at the same time the role of the prepreg layer also increases. Poisson's ratio v_{xy} reflects their common result. After the metal layer yields, Poisson's ratio v_{xy} of the GLARE gradually approaches that of the prepreg layer. As the layer ratio increases, the role of the prepreg layer becomes more prominent.

(4) The damage forms of the GLARE samples mainly include three types: overall delamination, fracture near the clamping point, and fracture in the middle. A small number of layers is more likely to delaminate, and a larger number of layers is more likely to cause overall fracture. For laminates with prepreg layers in the same direction, different numbers of layers cause slightly different damage mechanisms or degrees.

(5) The strain cloud diagram of the GLARE sample obtained by DIC method before fracture is consistent with the damage form of the prepreg layer obtained by corrosion delamination method. Therefore, comparing the forming processes of strain differences at key locations is helpful to study the damage mechanism and boundary effects of the prepreg layer.

Acknowledgments

This work was supported by the National Science and Technology Major Project (J2019-IV-0002-0069)

Author's Contribuitions: Conceptualization, Xie Liyang and Tong Anshi; Methodology, Tong Anshi and Zhang Jun; Investigation, Tong Anshi, Xie Liyang, Zhang Jun and Chen Ying; Writing-original draft preparation, Tong Anshi; Writing-review and editing, Tong Anshi, Xie Liyang and Wang Danfeng; Visualization, Tong Anshi; Supervision, Xie Liyang and Zhang Jun. All authors have read and agreed to the published version of the manuscript.

Editor: Pablo Andrés Muñoz Rojas

References

[1] Alderliesten, R. C., & Benedictus, R. (2008). Fiber/metal composite technology for future primary aircraft structures,J. Journal of Aircraft, 45(4), 1182-89.

[2] Botelho, E. C., Silva, R. A., Pardini, L. C., & Rezende, M. C. (2006). A review on the development and properties of continuous fiber/epoxy/aluminum hybrid composites for aircraft structures,J. Materials Research, 9, 247-56.

[3] Carrillo, J. G., & Cantwell, W. J. (2009). Mechanical properties of a novel fiber–metal laminate based on a polypropylene composite, J. Mechanics of materials, 41(7), 828-38.

[4] Bonhin, E. P., David-Müzel, S., de Sampaio Alves, M. C., Botelho, E. C., & Ribeiro, M. V. (2021). A review of mechanical drilling on fiber metal laminates, J. Journal of Composite Materials, 55(6), 843-69.

[5] Chen, Y., Liao, G., Ren, L., & Liu, X. (2018). Damage tolerance of GLARE laminates subjected to high-velocity impact, J. Acta Aeronautica et Astronautica Sinica, 39, 126-37.

[6] Nakatani, H., Kosaka, T., Osaka, K., & Sawada, Y. (2011). Damage characterization of titanium/GFRP hybrid laminates subjected to low-velocity impact,J. Composites Part A: Applied Science and Manufacturing, 42(7), 772-81.

[7] Hu, C., Sang, L., Jiang, K., Xing, J., & Hou, W. (2022). Experimental and numerical characterization of flexural properties and failure behavior of CFRP/Al laminates. Composite Structures, 281, 115036.

[8] Kadhim, M. M., & Alshamma, F. A. (2022). Investigation of analytical model of crack propagation under multi axial fatigue in fiber metal laminate,J. Composites Part C: Open Access, 9, 100305.

[9] Yao, L., Zhang, S., Cao, X., Gu, Z., Wang, C., & He, W. (2022). Tensile mechanical behavior and failure mechanisms of fiber metal laminates under various temperature environments, J. Composite Structures, 284, 115142.

[10] TONG, A. S., XIE, L. Y., LIU, J. Z., & ZHANG, X. C. (2017). Residual strength of notched fiber metal laminates, J. Journal of Northeastern University (Natural Science), 38(3), 375.

[11] He, W., Wang, C., Wang, S., Yao, L., Wang, L., & Xie, D. (2020). Characterizing and predicting the tensile mechanical behavior and failure mechanisms of notched FMLs—Combined with DIC and numerical techniques, J. Composite Structures, 254, 112893.

[12] Mercado, U. A., Sket, F., Wilde, F., Besel, M., & Requena, G. (2020). Determination of damage mechanisms and damage evolution in fiber metal laminates containing friction stir welded thin foils, J. International Journal of Materials Research, 111(1), 23-31.

[13] Zhang, J., Wang, Y., Yang, W., Dai, X., Zhao, Y., & Fang, G. (2023). Identifying the contributions of constituents to the fracture performance and failure mechanism of fiber metal laminate. Polymer Composites.

[14] Wu, G., & Yang, J. M. (2005). Analytical modelling and numerical simulation of the nonlinear deformation of hybrid fibre–metal laminates, J. Modelling and Simulation in Materials Science and Engineering, 13(3), 413.

[15] Carrillo, J. G., & Cantwell, W. J. (2007). Scaling effects in the tensile behavior of fiber-metal laminates, J. Composites Science and Technology, 67(7-8), 1684-93.

[16] Rajkumar, G. R., Krishna, M., Narasimhamurthy, H. N., Keshavamurthy, Y. C., & Nataraj, J. R. (2014). Investigation of tensile and bending behavior of aluminum based hybrid fiber metal laminates, J. Procedia Materials Science, 5, 60-68.

[17] Wang Shiyu(2012). Preparation and mechanical properties of fiber metal laminates Ph.D. Harbin,Harbin Institute of Technology. (in Chinese)

[18] Yang Wenke(2016). Experimental and Numerical Simulation on Mechanical Properties of Glare Fiber Metal Laminates Ph.D. Chang chun:Jilin University,2016. (in Chinese)

[19] Dadej, K., Bienias, J., & Surowska, B. (2019). On the effect of glass and carbon fiber hybridization in fiber metal laminates: Analytical, numerical and experimental investigation. Composite Structures, 220, 250-60.

[20] He, W., Wang, C., Wang, S., Yao, L., Wu, J., & Xie, D. (2020). Tensile mechanical behavior and failure mechanisms of multihole fiber metal laminates—experimental characterization and numerical prediction, J. Journal of Reinforced Plastics and Composites, 39(13-14), 499-519.

[21] Yao, L., Zhang, S., Cao, X., Gu, Z., Wang, C., & He, W. (2022). Tensile mechanical behavior and failure mechanisms of fiber metal laminates under various temperature environments, J. Composite Structures, 284, 115142.

[22] Yong, D. U., Yu'e, M. A., Wenbo, S. U. N., & Zhenhai, W. A. N. G. (2023). Effect of hygrothermal aging on moisture diffusion and tensile behavior of CFRP composite laminates, J. Chinese Journal of Aeronautics, 36(3), 382-392.

[23] Sun, J., Xu, S., Lu, G., Ruan, D., & Wang, Q. (2023). Mechanical response of fibre metal laminates (FMLs) under low to intermediate strain rate tension, J. Composite Structures, 305, 116493.

[24] Kötter, B., Karsten, J., Körbelin, J., & Fiedler, B. (2020). CFRP thin-ply fibre metal laminates: Influences of ply thickness and metal layers on open hole tension and compression properties,J. Materials, 13(4), 910.

[25] Xu, P., Zhou, Z., Liu, T., Pan, S., & Tan, X. (2022). In-situ damage assessment of FML joints under uniaxial tension combining with acoustic emission and DIC: Geometric influence on damage formation,J. Thin-Walled Structures, 170, 108515.

[26] Zheng, Y., Hu, K., Zhang, M., Zhu, J., Zhao, F., Han, W., Shi, Q. & Cao, Z. (2024). Characterizing damage patterns and evolution in Multi-Hole GLARE laminates under tensile load via integrated AE and DIC techniques, J. Composite Structures, 331, 117911.

[27] Jakubczak, P., Podolak, P., & Droździel-Jurkiewicz, M. (2023). The assessment of the compressive strength of fibre metal laminates after low-velocity impact, J. Composite Structures, 320, 117208.

[28] Serubibi, A., Hazell, P. J., Escobedo, J. P., Wang, H., Oromiehie, E., Prusty, G. B., Phillips, A. W., & St John, N. A. (2023). Fibre-Metal Laminate Structures: High-velocity impact, penetration, and blast loading-A review, Composites Part A: Applied Science and Manufacturing, 107674.

[29] Abhishek, S. K., Sunil Kumar, G., & Ramesh Kumar, R. (2021). DIC Correlation with Analysis Under Impact of Fiber Metal Laminates,J. In Advances in Production and Industrial Engineering: Select Proceedings of ICETMIE 2019 (pp. 335-345). Springer Singapore.

[30] Romanowicz, P. J., Szybiński, B., & Wygoda, M. (2024). Assessment of Digital Image Correlation Effectiveness and Quality in Determination of Surface Strains of Hybrid Steel/Composite Structures,J. Materials, 17(14), 3561.

[31] Lemmen, H. J. K., Alderliesten, R. C., Benedictus, R., Hofstede, J. C. J., & Rodi, R. (2008). The power of Digital Image Correlation for detailed elastic-plastic strain measurements. In WSEAS international conference on engineering mechanics, structures, engineering geology. Crate Island, Greece.

[32] Corr, D., Accardi, M., Graham-Brady, L., & Shah, S. (2007). Digital image correlation analysis of interfacial debonding properties and fracture behavior in concrete, J. Engineering Fracture Mechanics, 74(1-2), 109-121.

[33] Cantwell, W. J. (2000). The mechanical properties of fibre-metal laminates based on glass fibre reinforced polypropylene, J. Composites science and technology, 60(7), 1085-1094.